buildings

MDPI

Article

Analysis of Detailed and Simplified Finite Element Modelling Strategies for Simulating the Failure Behaviour of Timber Frame Diaphragms

Dries Byloos *, Tine Engelen and Bram Vandoren

Construction Engineering Research Group, Faculty of Engineering Technology, Hasselt University, Martelarenlaan 42, 3500 Hasselt, Limburg, Belgium; bram.vandoren@uhasselt.be (B.V.)
* Correspondence: dries.byloos@uhasselt.be

Abstract

Timber frame diaphragms play a central role in the lateral stability of modern timber buildings, yet current design codes insufficiently capture their nonlinear behaviour and governing failure mechanisms. This study evaluates two finite element modelling strategies to improve the prediction of diaphragm response. The first strategy, implemented in MATLAB®, explicitly models the nonlinear behaviour of sheathing-to-framing (STF) connections using an oriented orthogonal multilinear damage law. Validation against experimental tests on partially anchored and fully anchored diaphragms as well as in-plane bending specimens demonstrated accurate predictions of stiffness and force–displacement behaviour in both the linear-elastic and elastoplastic ranges. Deviations in peak load predictions for the detailed model reached up to approximately 25%, while stiffness predictions remained within approximately 10% of the experimental values. The second approach, implemented in commercial structural engineering software, represents STF connections by uncoupled elastoplastic spring elements. Although post-peak softening cannot be captured, peak capacities were predicted within approximately 3–5% for several configurations, with reliable stiffness estimates in most cases. A quantitative comparison using the normalised root mean square error between experimental and numerical force-displacement curves yielded values between approximately 5% and 14%, indicating good agreement between the numerical predictions and the experimental behaviour. Overall, the detailed model enables high-fidelity nonlinear analysis and insight into failure mechanisms, whereas the simplified spring approach offers a practical and computationally efficient modelling strategy suitable for routine engineering design.

Keywords: timber frame diaphragms; finite element modelling; spring elements; racking resistance; coupled damage-based multilinear evolution law; nonlinear modelling; simplified modelling

Academic Editors: Zhiyong Chen, Huazhang Zhou, Juan Carlos Pina and Christian Viau

Received: 4 March 2026
Revised: 11 March 2026
Accepted: 27 March 2026
Published: 30 March 2026

1. Introduction

With the increasing popularity of timber as a construction material comes a growing number of questions about its structural performance [1]. Timber is widely regarded as a material that reduces construction times compared to traditional materials, and a positive contribution to lowering CO_2 emissions [2,3]. These benefits make timber particularly attractive in the context of sustainable and efficient construction.

While timber frame systems have traditionally been used in low-rise buildings, recent developments show a clear shift toward their application in mid- and high-rise structures [4].

Such buildings, however, require more advanced structural assessments. Beyond ensuring local strength and stiffness of the structural components, aspects such as overall structural robustness and resistance to progressive collapse become increasingly critical [5]. Moreover, the demand for lateral stability in tall timber buildings often relies on lightweight timber frame diaphragms, which may include small or large openings. The design of these diaphragms is commonly guided by analytical methods described in the current Eurocode 5 [6]. Yet, the current [6] and even the forthcoming second-generation standard FprEN 1995-1-1 [7] are constrained by significant limitations. In particular, they cannot account for non-linear structural behaviour or wall-scale failure mechanisms. As a result, numerous practical design cases are overconservative, especially within the context of mid- and high-rise timber structures, and fall outside the boundaries of these codes.

To address this need, engineering practice could turn to finite element (FE) models. However, commonly used FE softwares used by practising engineers are typically limited to beam, column, and plate elements, making them incapable of adequately representing the behaviour of timber frame diaphragms, let alone modelling the non-linear failure behaviour.

A potential solution is to adopt more detailed modelling approaches that explicitly represent the components of timber frame diaphragms. In recent years, considerable research effort has focused on improving the numerical representation of timber shear walls and diaphragms, particularly regarding the nonlinear behaviour of sheathing-to-framing (STF) connections. Since the global response of timber frame systems is largely governed by the behaviour of these discrete fasteners, numerous studies have investigated modelling strategies to capture their stiffness, strength, and degradation characteristics.

Early modelling approaches typically represented STF connections using simplified spring elements calibrated from push-out tests [8,9], enabling efficient numerical simulation of wall behaviour. More advanced formulations were later developed to account for orthotropic effects and interaction between loading directions. For example, Vessby et al. [10] introduced coupled spring models that allow the representation of connection degradation and stiffness reduction under increasing deformation. These modelling strategies were subsequently refined by Humbert et al. [11], who proposed a versatile hysteretic constitutive law to provide a more robust numerical framework. Another advanced approach for representing STF connection behaviour is presented by Schweigler et al. [12], who developed a semi-analytical joint model based on kinematic compatibility and equilibrium considerations.

These modelling approaches for representing the sheathing-to-framing (STF) connection have formed the basis for many contemporary advanced simulation techniques [12–19], which are capable of predicting the stiffness, load-bearing capacity, and failure modes of timber frame walls. For instance, Kuai et al. [13,14,20] implemented coupled spring elements within the finite element software ABAQUS to simulate the lateral loading response of timber frame walls and modular timber structures, with particular emphasis on strength and failure behaviour. In contrast, Estrella et al. [21] demonstrated that a modelling approach employing three uncoupled springs, where the load–deformation behaviour of each STF connection is represented using a hysteretic constitutive model, can also provide relatively accurate predictions of the lateral response of timber frame walls.

Yet, such models usually require specialised software, advanced modelling expertise, and extensive computational resources, which restrict their usability in day-to-day engineering projects. Therefore, simplified modelling approaches that can be implemented in commonly used engineering software should be developed and validated. Such methods would enable engineering firms to analyse more complex structural situations in a reliable and computationally efficient manner.

Current literature addresses this gap in which a "mathematical method" has been developed, where diaphragm behaviour is represented through fictive diagonal members [22,23]. These approaches drastically reduce computational demand and required modelling expertise while still providing reliable results in many cases [24–28]. However, analysis using this method is limited to cases within the serviceability limit state, therefore not providing predictions of the load-bearing capacity, which is essential in structural design.

As mentioned above, a clear gap persists between advanced academic models and the tools available to practising engineers. Bridging this gap is essential to fully unlock the potential of timber in modern construction. To contribute to this effort, the presented research performs a comparative analysis of two types of FE approaches:

- A detailed damage-based model based on orthogonal coupling described in [9,10] referred to as "FEM1";
- An engineering-oriented model using uncoupled elastoplastic spring elements referred to as "FEM2".

The comparative analysis will be conducted by applying the two approaches within the development of timber diaphragm models and subsequently performing simulations. Section 2 presents a detailed description of the modelling strategies, while Section 3 outlines experimental campaigns [29–31] that serve as references for validation. The results obtained from the finite element analyses are compared and discussed in Section 4.

2. Materials and Methods

This section presents the two FE models employed for comparison in this study, with a summary of the methods and their key characteristics provided in Table 1. Secondly, two small-scale experimental campaigns focusing on characterizing connections' behaviour are discussed.

Table 1. Summarisation of the two different FE approaches.

	Coupled Damage Model (FEM1)	**Uncoupled Elastoplastic Model (FEM2)**
Studs and rails	Beam elements	Beam elements
Sheathing panels	Plane-stress continuum elements	Shell elements
STF connections	Oriented coupled spring elements	Uncoupled spring elements
Nonlinearity	Yes, damage law	Yes, elastoplastic law
Softening	Yes	No
FE Software	MATLAB®	Buildsoft Diamonds™

2.1. Detailed Modelling Approach (FEM1)

The detailed modelling approach, based on a coupled damage model, is implemented in MATLAB® (version 2025) to enable 2D analysis of timber diaphragms. The modelling framework includes a user-friendly interface where users can define diaphragm dimensions, connection spacing, support conditions, openings, and loading scenarios. Both displacement- and force-controlled analyses can be performed by applying imposed displacements or forces. In addition, the interface provides a visualisation of the diaphragm, including the STF connections, support conditions, and applied loads, as illustrated in Figure 1.

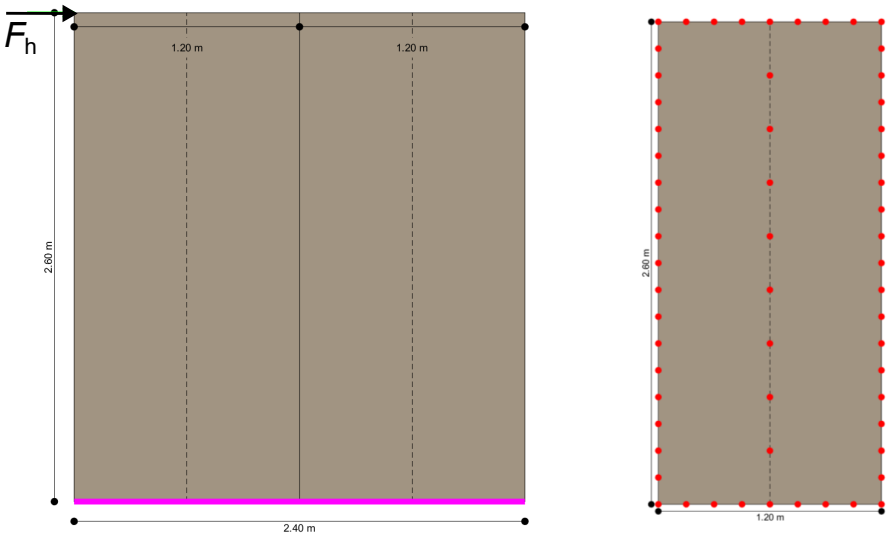

Figure 1. Visualisation of the diaphragms presented in FEM1. The purple line represents the fixed lower rail of the wall assembly, restraining it from undergoing deformation.

The FE framework employs a Newton–Raphson iterative scheme to solve the system of nonlinear equations arising from the discretisation. Nonlinearity in the model originates solely from the STF connections, which are represented as nonlinear spring elements. The timber frame is modelled with linear-elastic beam elements, while the sheathing panels are represented as linear-elastic plane-stress continuum elements [32]. In the case of fully anchored diaphragms (i.e., the leading stud is directly connected to the foundation via a tie-down), the stud-to-rail connections in the leading stud are modelled as hinges, representing the physical tie-down allowing for the direct transfer of the tensile forces at this location. For partially anchored diaphragms (i.e., without a tie-down on the leading stud), the connection is represented by a spring that simulates the elastic withdrawal stiffness of the connection between the leading stud and the bottom rail.

As stated earlier, the nonlinearity of the model results from the STF connections, which are modelled using a set of nonlinear springs. The nonlinear springs are calibrated using connection experiments with a least five specimens [33], which provide force-displacement diagrams. The experiments are performed parallel (yielding an elastic stiffness $K_{\mathrm{SLS,par}}$) and perpendicular (yielding an elastic stiffness $K_{\mathrm{SLS,perp}}$) to the grain of the timber element, capturing the orthotropic behaviour of the timber. The experimental setups are discussed in Section 2.4. The force-displacement diagrams gathered from a test (with loading parallel or perpendicular to the grain) are used to determine an overall average experimental force-displacement diagram, which is further segmented using linear lines to create a multilinear law that represents the behaviour of the connector in that specific direction. The number of segments chosen was seen not to influence the results; however, it is preferred to have the minimum number of segments (which still accurately represent the observed average force-displacement diagram) possible to optimise the model. Examples of this segmentation can be found in Appendix A.

Box 1 presents the step-by-step algorithm for implementing an elasticity-based damage model, which is used in every STF in the detailed modelling framework. The procedure starts by, for every increment j+1, computing the updated total displacement field $\mathbf{u}_{j+1}$ based on the incremental displacement field $\mathbf{\Delta u}_{j+1}$. The vector $\mathbf{u}_{j+1}$ contains all degrees of freedom of the system, including the displacements on the frame side of the STF connections, denoted $u_{\mathrm{par,frame}}$ or $u_{\mathrm{perp,frame}}$, and the displacements on the sheathing panel side of the STF connections, denoted $u_{\mathrm{par,panel}}$ or $u_{\mathrm{perp,panel}}$. The slips s_{par} are the vertical displacements in case of STF connections on the studs, or the horizontal displacements in

case of STF connections on the rails. Similarly, s_{perp} denotes the horizontal displacements in case of STF connections on the studs and the vertical displacements in case of connections on the rails.

Box 1. Algorithmic treatment of coupled damage model, at the level of an STF connection.

Steps related to the Newton–Raphson algorithm, i.e., the iterative loop and the calculation of the consistent tangent matrix, are omitted for clarity.
For every increment $j+1$:

1. Compute the updated total displacement field:
   $\mathbf{u}_{j+1} = \mathbf{u}_j + \mathbf{\Delta u}_{j+1}$
2. Compute, per direction, the respective slip of each STF connector:

Parallel	**Perpendicular**
$s_{par,j+1} = u_{par,frame,j+1} - u_{par,panel,j+1}$	$s_{perp,j+1} = u_{perp,frame,j+1} - u_{perp,panel,j+1}$

3. Compute the orientation of the initial displacement trajectory of the respective spring (fixed throughout the entire analysis and determined in increment 1): ϕ
4. Evaluate the damage loading functions by using the internal history variable κ:

Parallel	**Perpendicular**
$f_{par} = s_{par,j+1} - \kappa_{par,j}$	$f_{perp} = s_{perp,j+1} - \kappa_{perp,j}$
if $f_{par} \geq 0$, $\kappa_{par,j+1} = s_{par,j+1}$	if $f_{perp} \geq 0$, $\kappa_{perp,j+1} = s_{perp,j+1}$
else $\kappa_{par,j+1} = \kappa_{par,j}$	else $\kappa_{perp,j+1} = \kappa_{perp,j}$

5. Update the damage variables using the quadratic interaction formula from [10] and shown in Equations (1) and (2):

Parallel	**Perpendicular**
$\omega_{par,j+1} = \omega(\kappa_{par,j+1}, \kappa_{perp,j+1})$	$\omega_{perp,j+1} = \omega(\kappa_{perp,j+1}, \kappa_{par,j+1})$

6. Compute the resulting secant stiffness of each respective loading direction:

Parallel	**Perpendicular**
$K_{par,j+1} = (1 - \omega_{par,j+1}) K_{par,SLS}$	$K_{perp,j+1} = (1 - \omega_{perp,j+1}) K_{perp,SLS}$

7. Assemble new stiffness matrices according to the oriented spring pair method [9]

From this vector, the slip for both loading directions (parallel and perpendicular to the grain), is subsequently determined by using the respective displacement in each direction. Afterwards, a parameter ϕ is determined, representing the initial loading direction of each spring element and fixed throughout the analysis, calculated in increment 1. Following this, the damage loading function (f) is evaluated. This function determines whether the internal history variable κ increases or remains unchanged, depending on whether the loading condition is met. As two damage-driving parameters are defined, both κ_{par} and κ_{perp} are evaluated with respect to the respective loading function. Once the loading state is determined, the damage variable ω is updated accordingly. Because stiffness is assessed in two orthogonal loading directions, the damage variable is represented by two components: the parallel component (ω_{par}) and the perpendicular component (ω_{perp}). Equation (1) describes the procedure used to compute ω_{par}, while Equation (2) presents an analogous formulation for ω_{perp}. The parameters κ^*_{par} and κ^*_{perp} appearing in Equations (1) and (2) denote scaled (equivalent) connection slips, obtained via the quadratic coupling relation (ellipse) proposed by Vessby [10]. The parameters m and n correspond to the vertices of the multilinear constitutive laws derived from experimentally obtained force-displacement relationships for each respective loading direction.

$$\omega_{par} = 1 - \frac{1}{K_{SLS,par}\,\kappa^*_{par}} \left[\frac{F_{par,n+1} - F_{par,n}}{\kappa_{par,n+1} - \kappa_{par,n}} \left(\kappa^*_{par} - \kappa_{par,n} \right) - F_{par,n} \right] \tag{1}$$

$$\omega_{perp} = 1 - \frac{1}{K_{SLS,perp}\,\kappa^*_{perp}} \left[\frac{F_{perp,m+1} - F_{perp,m}}{\kappa_{perp,m+1} - \kappa_{perp,m}} \left(\kappa^*_{perp} - \kappa_{perp,m} \right) - F_{perp,m} \right] \tag{2}$$

Figure 2 visualises the interaction between the parallel and perpendicular damage directions, highlighting how the combined evolution of ω_{par} and ω_{per} governs the overall stiffness degradation.

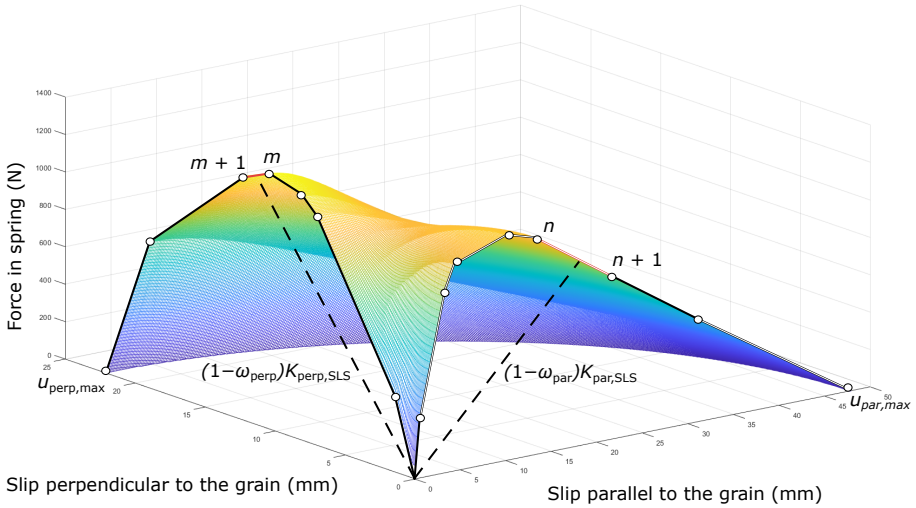

Figure 2. A 3D representation of the STF connections' force-slip behaviour based on the coupled damage-based multilinear evolution law. In this representation, a multilinear evolution law (and its unloading branch) for loading parallel to the grain is indicated, where *n* and *m* denote a vertex of the multilinear law.

Once the damage variables are determined, the resulting secant stiffnesses for each direction are computed by reducing the elastic stiffness proportionally to the current damage state. Finally, the new stiffness matrix is constructed using the newly defined $K_{par,j+1}$ and $K_{perp,j+1}$ following the oriented spring pair method from [9], in which each connector is oriented according to its initial displacement trajectory determined in increment 1 (ϕ). Since a damage-based approach is adopted, permanent deformation (after unloading) is not captured by this method, and unloading returns to the point of origin (no residual slip). In the algorithm box, steps related to the Newton–Raphson procedure, namely the iterative loop and the construction of the consistent tangent matrix, are omitted for clarity. For these aspects, the reader is referred to, for example, de Borst et al. [34].

This modelling strategy is referred to as the detailed approach due to the complexity of incorporating detailed STF connection behaviour within the numerical model. Although, as illustrated in Appendix C, the total number of mesh elements or nodes generated in this approach is lower than in FEM2, the computational demand of FEM1 is higher. This increased computational effort is primarily attributed to the Newton–Raphson iterative procedure employed in the analysis.

2.2. Simplified Modelling Approach (FEM2)

The second modelling strategy is implemented using the structural engineering software Buildsoft Diamonds™ [35]. The software facilitates the analysis of structural elements such as beams, shells, and semi-rigid links, the latter represented as spring elements. In this FE model, spring elements are introduced to simulate STF connections. These springs are assigned specific stiffness values that, depending on the selected modelling approach, either exhibit purely elastic behaviour or account for plastic deformations up to the peak load. Failure is not explicitly modelled, as the post-peak softening of the connections cannot be captured within this framework. Due to this modelling limitation, the observed response will generate a plateau-like curve at peak capacity within the force-displacement diagrams.

The adopted approach employs uncoupled orthogonal spring elements, allowing the model to reproduce the behaviour both parallel and perpendicular to the grain direction. However, because the spring elements are uncoupled (a limitation of the software), this method may lead to an overestimation of stiffness in the inelastic range, under certain loading conditions, as reported by [10]. The stud-to-rail connection is defined in a similar manner as in the previous section, either as a fully rigid connection or as a spring element characterised by its withdrawal stiffness.

This modelling strategy is referred to as the simplified modelling approach, as it employs a simplified representation of the STF connection behaviour and can be implemented using the user-friendly interface of commonly used structural engineering software. In addition, it requires limited modelling or mathematical expertise from the user and involves significantly lower computational demand, approximately 8 times faster than FEM1 on average.

2.3. Stud-to-Rail Connection Experiment

The withdrawal stiffness of the connection used in the studs-to-rail connection for partially anchored walls is experimentally obtained using the test setup shown in Figure 3, where a single nail connection is embedded in a timber element. In this setup, the top of the connector is secured between two clamps, and a vertical upward force is applied to induce withdrawal. The resulting stiffness value for a single connector is multiplied by the number of connectors used in the actual connection. The dimensions of the nail and the timber material can be found in Table 2, while the experimental data obtained is shown in Appendix B.

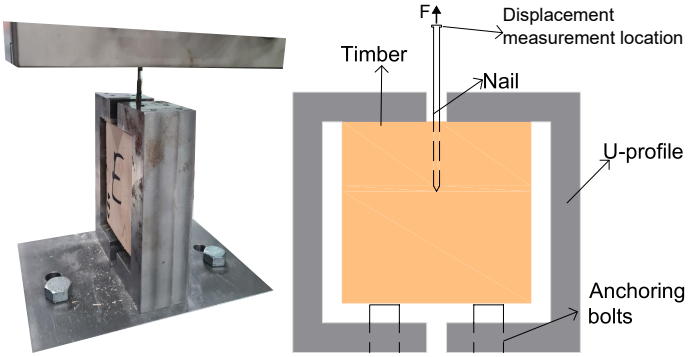

Figure 3. Withdrawal experiment on a single nail connection, (**left**) picture of the test setup, and (**right**) technical drawing of the test setup.

Table 2. Materials and dimensions of the partially anchored timber frame diaphragms used in the experimental campaign [29].

Component	Material/Type	Dimensions/Details
Framing (studs & rails)	C24 softwood	50 × 70 mm cross-section and density 350 kg/m^3
Diaphragm length (rails)	-	600 mm (1–4 panels: 600–2400 mm total)
Diaphragm height	-	1400 mm
Stud spacing on outer studs	-	300 mm
Stud-to-rail connection	Nails	Ø3 mm × 80 mm, 2 nails per joint
Sheathing panels	Particle board (type P5)	12 mm thickness
Sheathing-to-framing connection	Coated staples	1.70 × 1.88 mm legs, 50 mm length
Fastener spacing	-	150 mm
Anchorage	Screws	3 screws in first 300 mm of bottom rail, then 2 screws every 300 mm
Openings	Door and window	Door height: 1075 mm; Window height: 575 mm

2.4. Sheathing-to-Framing Connection Experiment

To characterise the shear capacity of the STF connectors, two series of monotonic push-out tests were conducted. During which monotonic vertical loading was used until reaching failure, the displacement of the specimens was measured at the load application point (which corresponds to the top of the timber element). The series consisted of experiments both parallel and perpendicular to the grain of the timber element, shown in Figure 4. The small-scale experiments consist of two connectors on each side, which connect the sheathing panel to the timber element. The STF connection type and timber materials vary by tested configuration and are listed in Tables 2–4. The moisture content of the timber framing elements was not explicitly measured; however, they were kept in a constant laboratory environment at 20 °C and 60% relative humidity. Due to the number of STF connection experiments and to not overcrowd the article, the results are shown in Appendix A.

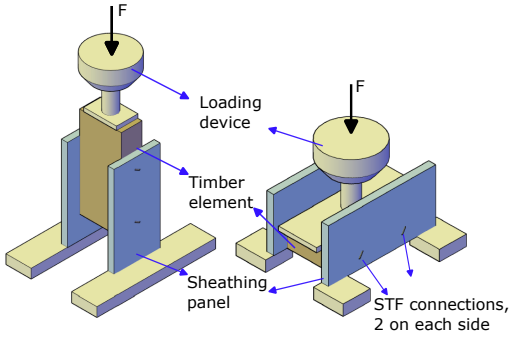

Figure 4. Push-out connection experiment, (**left**) parallel to the grain, and (**right**) perpendicular to the grain.

Table 3. Materials and dimensions of the fully anchored timber frame wall diaphragms used in the experimental campaign [30].

Component	Material/Type	Dimensions/Details
Framing (studs & rails)	C18 softwood	45 × 95 mm cross-section and density 320 kg/m^3
Diaphragm length (rails)	-	2400 mm
Diaphragm height	-	2600 mm
Stud spacing	-	600 mm
Stud-to-rail connection	Nails	Ø2.8 mm × 80 mm, 3 nails per joint
Sheathing panels	Structural gypsum plasterboard A & B, Resinoid-bonded particle board Non-load-bearing gypsum plasterboard	12.5 mm thickness (EN 520+A1) 12 mm thickness (EN 13986+A1) 12.5 mm thickness
Sheathing configuration	Single/Double (stacked)	8 configurations tested
Sheathing-to-framing connection	Coated staples	Type a: 1.53 × 1.53 mm legs, crown 10.6 mm, length 44 mm Type b: 1.88 × 1.70 mm legs, crown 11.4 mm, length 50 mm Type c: 1.83 × 1.83 mm legs, crown 10.6 mm, length 44 mm

Table 4. Materials and dimensions of the timber frame diaphragms used in the in-plane bending experimental campaign [31].

Component	Material	Dimensions/Details
Framing (studs & rails)	C24 softwood	45 × 95 mm cross-section and density 350 kg/m^3
Diaphragm length (rails)	-	3420 mm
Diaphragm height	-	1200 mm
Stud spacing	-	570 mm
Stud-to-rail connection	Nails	Ø2.8 mm × 80 mm, 3 nails per joint
Sheathing panels	Oriented strand board (OSB3)	12.5 mm thickness
Sheathing-to-framing connection A	Screws	5 mm × 80 mm, predrilled (3 mm)
Sheathing-to-framing connection B	Coated staples	1.88 × 1.70 mm legs, 11.4 mm crown, 50 mm length, stapled at 30°

3. Validation Experiments on Wall Diaphragms

The accuracy of the different modelling approaches is assessed through validation against multiple specimens from different experimental campaigns reported in [29–31], conducted by the authors. This section provides a concise overview of the experimental programs, including the specimen dimensions and the materials employed. For a more detailed description and in-depth discussion, the reader is referred to the respective original research articles. For the first experimental campaign, the tests described in Section 2.3 were conducted. The experiments presented in Section 2.4 were also performed, but in this case, they were carried out across all three experimental campaigns, each time employing the materials specific to the respective campaign. To not overcrowd the article, the results of the different experiments are shown in Appendices A and B.

3.1. Racking Resistance of Partially Anchored Wall Diaphragms

The experimental campaign investigated the racking resistance of partially anchored timber frame wall diaphragms. In total, eleven different diaphragm configurations were tested, some with door or window openings and some subjected to additional vertical loading. Since the experiments were not the main focus of [29], a more in-depth overview is given below and in Table 2; however, additional information can still be found in the original research article.

Each diaphragm was constructed with C24 softwood members of 50 × 70 mm cross-section, arranged into panels of 1400 mm height and 600 mm width. Up to four panels were connected side by side, resulting in total diaphragm lengths ranging from 600 to 2400 mm. Vertical studs were spaced at 300 mm intervals. The sheathing consisted of 12 mm thick particle boards of type P5 [36], which were attached to the frame using staples with leg dimensions of 1.70 × 1.88 mm and 50 mm in length. The mechanical properties of the P5 sheathing panels are 9.4 N/mm^2 for the tensile strength, 2000 N/mm^2 for the modulus of elasticity, and 960 N/mm^2 for the shear modulus. The fastener spacing on the sheathing panel was 150 mm. Anchorage of the framing to the foundation was achieved through screws: three screws were installed within the first 300 mm of the bottom rail, with two additional screws placed every 300 mm along the remaining length. Several diaphragm configurations contained openings. Door openings were 1075 mm in height, whereas window openings had a height of 575 mm. For three configurations, an additional vertical load of 1.75 kN was applied to the leading stud using weighted straps, in order to study the effect of partial anchorage reinforcement. Drawings of each tested configuration can be found in Section 3 of [29], and a picture of the test setup is shown in Figure 5.

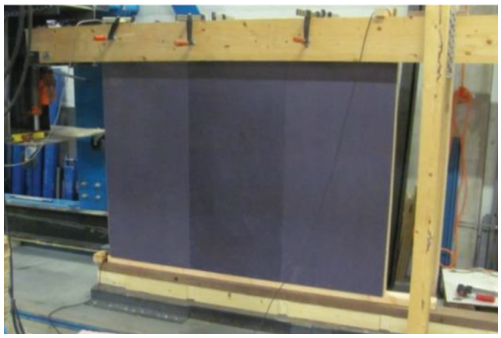

Figure 5. Picture of the test setup of the partially anchored wall diaphragm experiment [29].

3.2. Racking Resistance of Fully Anchored Wall Diaphragms

The experimental campaign (Figure 6) within [30] focused on the investigation of the racking resistance of fully anchored timber frame diaphragms with both single- and double-layered sheathing systems. Eight different wall configurations were constructed

and tested under monotonic horizontal loading in accordance with EN-594 [37]. The dimensions and materials employed can be found in Table 3. The sheathing of the diaphragms varied depending on the configuration. Three types of panels were employed. Connections between the sheathing and the timber framing were realised with coated staples. The configurations used for comparison in this study are limited to single-layered sheathing configurations using two types of gypsum plasterboards [38], referred to as type A or B. The mechanical properties of the gypsum plasterboard A are 2.1 N/mm^2 for the tensile strength, 2300 N/mm^2 for the modulus of elasticity, and 1750 N/mm^2 for the shear modulus. Gypsum plasterboard B has 3.91 N/mm^2 for the tensile strength, 2270 N/mm^2 for the modulus of elasticity, and 1775 N/mm^2 for the shear modulus. The last gypsum plasterboard is a non-load-bearing panel, for which the mechanical properties were not determined due to its non-load-bearing nature.

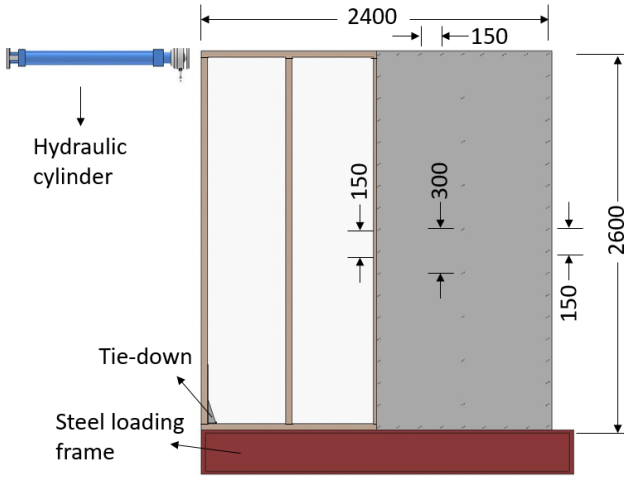

Figure 6. Diaphragm configuration tested within [30]. Dimensions in mm.

3.3. In-Plane Bending Resistance of Wall Diaphragms

Five timber-frame diaphragms were tested under four-point in-plane bending. Two diaphragms were sheathed on both sides with OSB3 panels fastened by staples, two diaphragms were sheathed on both sides with OSB3 panels fastened by screws, and one diaphragm was sheathed on only one side with screw fasteners. The used materials and dimensions can be found in Table 4, and a visualisation of the tested walls can be found in Figure 7. The mechanical properties of the OSB3 sheathing panels are 9.4 N/mm^2 for the tensile strength, 3500 N/mm^2 for the modulus of elasticity, and 1080 N/mm^2 for the shear modulus. For further clarification of the geometries, dimensions, and results, the reader is referred to the study conducted by Byloos et al. [31].

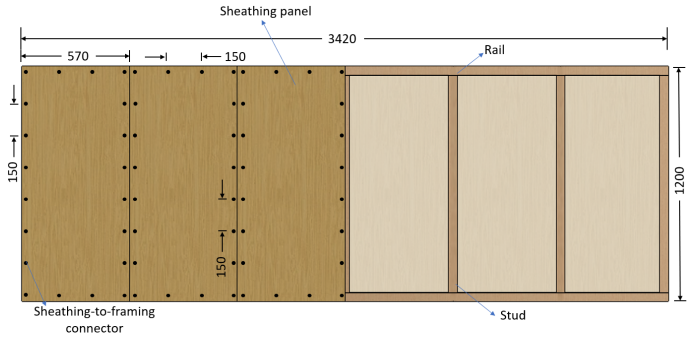

Figure 7. Diaphragm configuration tested within [31]. Dimensions in mm. Reprinted with permission from Ref. [31] Copyright year 2026 and Copyright Owner's Name Dries Byloos

4. Comparison of Numerical and Experimental Data

The numerical and experimental results are compared by evaluating the peak load attained in each test and the racking stiffness within the linear portion of the force-displacement response. The racking stiffness is determined in accordance with EN 594 [37], where the stiffness is calculated using the force and corresponding displacement measured at 20% and 40% of the peak load.

4.1. Racking Resistance of Partially Anchored Wall Diaphragms

Figure 8 compares experimental and numerical force-displacement responses for both increased wall lengths and walls with door and window openings. A quantitative summary of stiffness, peak capacity, and displacement deviations is provided in Table 5. A visualisation of how the FE model visualises the data is shown in Appendix C.

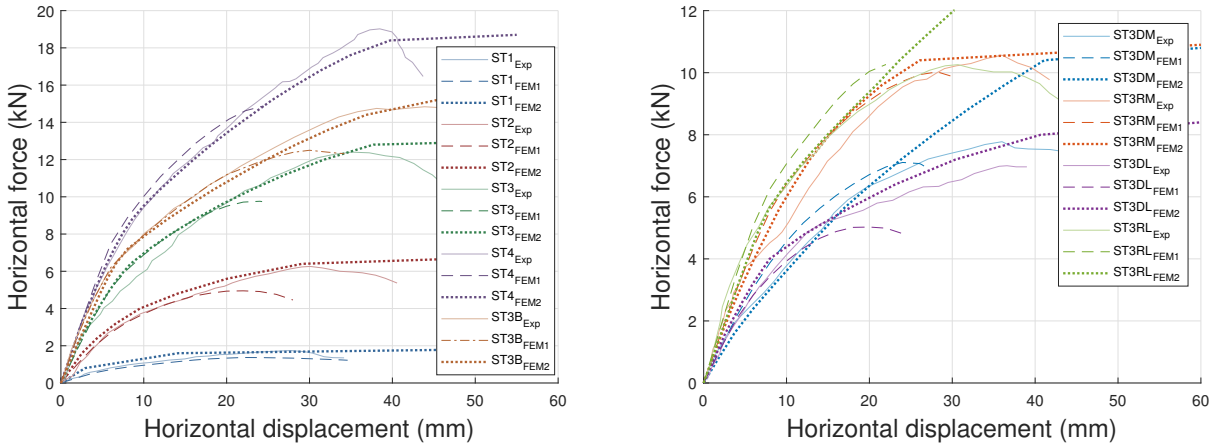

Figure 8. Comparison between experimental force–displacement responses of the partially anchored experiments and the numerical simulations obtained with FEM1 and FEM2. Solid lines represent the experimental measurements from [29], while markers indicate the numerical predictions of the two modelling strategies. (**a**) Increasing diaphragm length and (**b**) influence of openings.

Table 5. Comparison of FEM1 and FEM2 predictions with experimental results from the partially anchored timber frame wall diaphragms [29].

Configuration	Parameter	FEM1 Deviation	FEM2 Deviation
Increasing diaphragm length	Racking stiffness	+10%	+5%
	Peak capacity	−23%	+3%
Door opening (first panel)	Racking stiffness	+7%	+21%
	Peak capacity	−40%	+12%
Door opening (center panel)	Racking stiffness	+7%	−21%
	Peak capacity	−9%	+27%
Window (first panel)	Racking stiffness	+4%	+12%
	Peak capacity	−2%	+27%
Window (center panel)	Racking stiffness	+20%	−12%
	Peak capacity	−7%	+3%

The left diagram in Figure 8 compares experimental and numerical force-displacement responses for increasing wall lengths. FEM1, which employed coupled spring behaviour, reproduced the initial linear-elastic and elastoplastic response with good accuracy, but consistently predicted failure at lower displacements. Deviations in peak capacity reached

approximately 25%. FEM2 showed similar racking stiffness with only minor deviations of about 4%. Peak capacity was predicted with higher accuracy, differing on average by 3% from experimental results. However, as FEM2 does not incorporate post-peak softening, the force-displacement response remained constant beyond peak capacity, preventing simulation of actual failure.

The second force-displacement graph in Figure 8 presents the response for diaphragms with door and window openings. FEM1 showed deviations in racking stiffness of 7% for specimens with door openings, 4% for specimens with a window in the first sheathing panel, and 20% for specimens with a centrally located window opening. Peak capacity predictions were more accurate for diaphragms with window openings than for those with doors. In all cases, failure was predicted at lower displacements than observed experimentally. FEM2 exhibited larger discrepancies. For specimens with door openings, racking stiffness deviated by 21%, while window specimens deviated by 12%. Peak capacity predictions differed by an average of 27% for the specimen with a window in the first panel and the specimen with a centrally located door opening, while the remaining specimens deviated by approximately 12%.

4.2. Racking Resistance of Fully Anchored Diaphragms

Figure 9 and Table 6 compare experimental and numerical force–displacement responses for wall configurations 1 and 4. Since, for each configuration, multiple specimens were tested, an average of the three specimens is taken for comparison with the FE models. A visualisation of how the FE model visualises the data is shown in Appendix C.

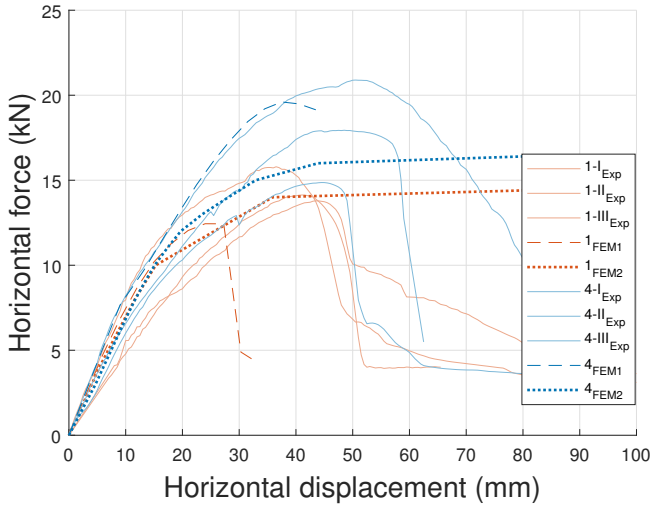

Figure 9. Comparison between experimental force-displacement responses of the fully anchored experiments and the numerical simulations obtained with FEM1 and FEM2. Solid lines represent the experimental measurements from [30], while markers indicate the numerical predictions of the two modelling strategies.

Table 6. Comparison of FEM1 and FEM2 predictions with experimental results from the fully anchored timber frame wall diaphragms [30].

Configuration	Parameter	FEM1 Deviation	FEM2 Deviation
1	Racking stiffness	+10%	+5%
	Peak capacity	−16%	−3%
4	Racking stiffness	+10%	+5%
	Peak capacity	+11%	−3%

For configuration 1, FEM1 reproduced the initial stiffness reasonably well but consistently underestimated displacement at peak force. Peak capacity predictions deviated by approximately 16% compared to experimental values. FEM2 provided a closer approximation of both stiffness and peak capacity, with deviations of less than 5%, although post-peak softening was not captured as mentioned previously.

For configuration 4, FEM1 again matched the initial stiffness but underpredicted ultimate displacement, with peak force values deviating by around 11%. FEM2 demonstrated improved accuracy in peak capacity, with deviations below 5% while still accurately predicting the racking stiffness.

4.3. In-Plane Bending Resistance of Scaled Diaphragms

Figure 10 compares experimental and numerical force-displacement responses from the in-plane bending experiments. A quantitative summary of stiffness and peak capacity deviations is provided in Table 7. A visualisation of how the FE model visualises the data is shown in Appendix C.

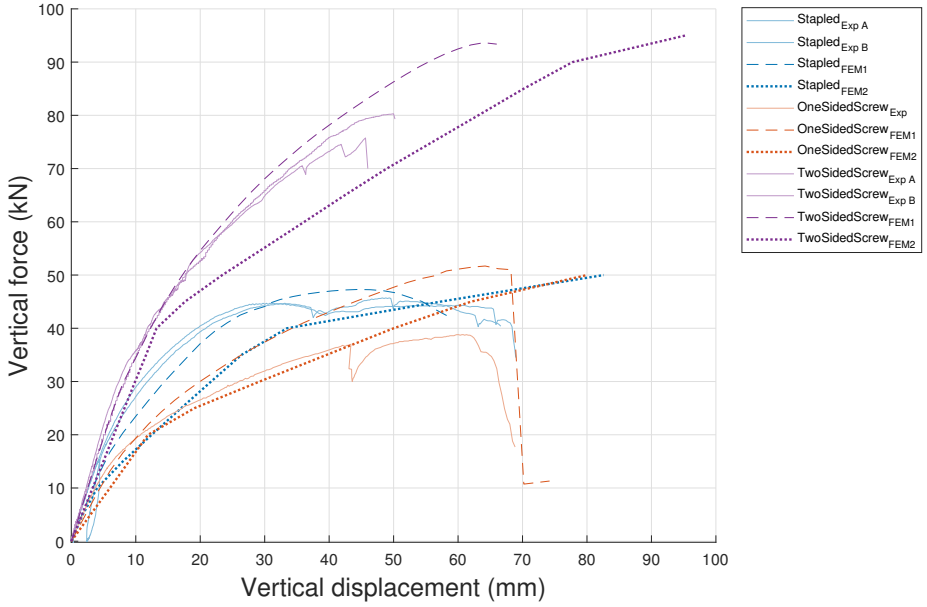

Figure 10. Comparison between experimental force–displacement responses of the bending experiments and the numerical simulations obtained with FEM1 and FEM2. Solid lines represent the experimental measurements from [30], while markers indicate the numerical predictions of the two modelling strategies.

Table 7. Comparison of FEM1 and FEM2 predictions with experimental results from the in-plane bending experiments [31].

Configuration	Parameter	FEM1 Deviation	FEM2 Deviation
Stapled	Stiffness	−11%	−55%
	Peak capacity	+5%	+11%
One-sided screw	Stiffness	−17%	−60%
	Peak capacity	+30%	+16%
Two-sided screw	Stiffness	−5%	−23%
	Peak capacity	+19%	+15%

For the stapled configuration, FEM1 reproduced both stiffness and peak capacity with relatively good accuracy, deviating by 11% and 5%, respectively. FEM2, in contrast, showed a larger stiffness deviation of 55% and an 11% difference in peak capacity.

For the one-sided screw specimens, FEM1 underestimated stiffness by 17% and overpredicted peak capacity by 30%. FEM2 exhibited even larger stiffness deviations (60%) but provided closer agreement in peak capacity, with a deviation of 16%.

For the two-sided screw specimens, FEM1 showed deviations of 5% in stiffness and 19% in peak capacity. FEM2 produced less accurate stiffness predictions (23% deviation) but slightly improved peak capacity predictions, differing by 15% from the experimental results.

4.4. Performance of the FE Models

Across all investigated test types, consistent trends were observed in the performance of the two numerical modelling strategies. FEM1 generally reproduced the initial stiffness with reasonable accuracy and provided reliable predictions of racking stiffness, particularly in configurations with openings. However, it systematically underestimated peak capacity and ultimate displacement. FEM2, in contrast, yielded closer agreement with experimental peak capacities, especially for longer diaphragm configurations and screwed connections, but its stiffness predictions were less reliable in several cases. A common limitation of FEM2 was the absence of post-peak softening, which led to unrealistic plateaus in the force-displacement response. Overall, FEM1 proved more robust in capturing stiffness, whereas FEM2 was more accurate in predicting peak capacity, while still remaining reasonably accurate in stiffness.

To provide a more rigorous assessment of the predictive accuracy of the numerical models, the normalised root mean square error (NRMSE) between the experimental and numerical force-displacement curves was calculated, and shown in Table 8. Prior to the calculation, the force responses were normalised with respect to their respective peak loads in order to evaluate the similarity of the response shape independently of absolute force levels. To ensure a fair comparison, the calculation was performed for data points up to the peak force.

$$\mathrm{NRMSE} = \frac{\sqrt{\frac{1}{n}\sum_{i=1}^{n}\left(F_{\mathrm{exp},i} - F_{\mathrm{num},i}\right)^2}}{F_{\mathrm{exp,max}}} \tag{3}$$

where $F_{\mathrm{exp},i}$ and $F_{\mathrm{num},i}$ denote the experimental and numerical force values at displacement point i, n is the number of sampled points along the force-displacement curve (a point was taken each 2 mm), and $F_{\mathrm{exp,max}}$ is the maximum experimental force used for normalisation.

Table 8. Comparison of the average NRMSE values calculated based on the FEM1 and FEM2 responses.

Test Type	FEM1	FEM2
Partially anchored	5.2%	5.0%
Fully anchored	14.2%	10.9%
In-plane bending	11.6%	13.6%

The calculated NRMSE values confirm the trends observed in the comparison of stiffness and peak load predictions. For the partially anchored wall diaphragms, both modelling approaches show very low NRMSE values of approximately 5%, indicating a strong agreement between the numerical and experimental force-displacement responses. This suggests that both models can reproduce the overall response shape for these configurations. For the fully anchored diaphragms, slightly higher NRMSE values are observed, with FEM1 reaching 14.2% and FEM2 10.9%.

For the in-plane bending tests, both approaches again yield moderate NRMSE values of approximately 11–14%. FEM1 captures the stiffness-dominated response slightly better, while FEM2 shows somewhat larger deviations due to the simplified, uncoupled spring representation of the connections. Overall, the NRMSE analysis confirms that both mod-

elling approaches reproduce the global force-displacement behaviour with good accuracy, while highlighting the trade-off between modelling detail and computational efficiency.

Due to the promising results and the simplified modelling strategy adopted in FEM2, the approach lends itself to potential upscaling to full-scale structural systems. This would allow the model to incorporate adjacent wall and roof elements, enabling building-level simulations. Such an extension would also facilitate direct comparison between numerical predictions and full-scale experimental results obtained at the structural system level.

5. Conclusions

This study evaluated two finite element modelling strategies for timber frame diaphragms: a more advanced modelling strategy implemented in MATLAB®(FEM1) and an engineering-oriented modelling strategy, which can be implemented in common engineering software (FEM2). The first approach, FEM1, employed an oriented orthogonal multilinear damage law to characterise the sheathing-to-framing connections, enabling the model to capture stiffness degradation and predict failure. The second approach, FEM2, implemented uncoupled orthogonal spring elements within a standard engineering software, providing a more practical and computationally efficient method, but without the ability to reproduce softening behaviour.

The predictive capabilities of both methods were assessed through comparisons with three experimental campaigns: (i) racking resistance of partially anchored diaphragms, (ii) racking resistance of fully anchored diaphragms, and (iii) in-plane bending of diaphragms with stapled and screwed connections. The results highlight distinct strengths and limitations of each modelling strategy.

Across the racking tests, FEM1 consistently reproduced the initial linear-elastic and elastoplastic response with reasonable accuracy. Stiffness predictions were generally reliable, including for specimens with door and window openings. However, FEM1 tended to underestimate peak capacity and ultimate displacement. In contrast, FEM2 provided more accurate predictions of peak load capacity, particularly for longer diaphragm configurations and screwed connections, with deviations typically below 5%. Nevertheless, stiffness predictions were less consistent with the addition of openings, causing more deviations, and the absence of softening led to unrealistic plateaus beyond peak capacity.

The in-plane bending experiments further reinforced these observations. FEM1 showed closer agreement with experimental stiffness, while FEM2 offered improved predictions of peak capacity for screwed specimens but systematically overestimated stiffness in stapled and one-sided screw configurations. These differences reflect the fundamental trade-off between a detailed but computationally demanding mesoscale formulation and a simplified uncoupled spring-based approach suitable for integration into commercial engineering software.

The additional NRMSE analysis confirmed that both modelling approaches reproduce the global force-displacement response with reasonable accuracy, with deviations typically ranging from 5% to approximately 15%, which indicates good agreement between predictions and results.

Overall, the findings demonstrate that FEM1 is more robust in capturing stiffness and displacement behaviour, making it suitable for advanced research applications where detailed failure mechanisms are of interest. FEM2, while having more variation in stiffness prediction, is advantageous for engineering practice due to its ease of implementation and efficiency, particularly when the focus is on estimating peak capacities or stiffness within horizontal loading applications.

Future work should focus on bridging the gap between these approaches by extending simplified models to incorporate post-peak softening while maintaining computational efficiency. Additional upscaling of FEM2 to include multiple adjacent walls or floors and

validate these results with full-scale structure experiments will also be essential to ensure the transferability of the methods to mid- and high-rise timber frame buildings.

Author Contributions: D.B.: Writing—original draft, Writing—Review and Editing, Visualisation, Validation, Methodology, Investigation, Formal analysis. T.E.: Investigation, Writing—Review and Editing. B.V.: Writing—original draft, Writing—Review and Editing, Supervision, Resources, Project administration, Funding acquisition, Conceptualisation. All authors have read and agreed to the published version of the manuscript.

Funding: The authors gratefully thank the Special Research Fund (BOF) of Hasselt University for supporting this research. BOF reference: BOF22OWB18. Secondly, the authors also acknowledge the Flemish Agency for Innovation and Entrepreneurship (VLAIO) Technology Transfer Program (TETRA) for funding the HoP_HoVer project (VLAIO reference: HBC.2023.0066) and the HSBNext project (VLAIO reference: HBC.2020.2098).

Data Availability Statement: Data will be made available upon request.

Acknowledgments: The authors acknowledge the work of Dan Dragen, Kenny Reweghs, Niels Blocken, and WOOD.be, who helped perform the experiments.

Conflicts of Interest: The authors declare no conflicts of interest.

Appendix A. Sheathing-to-Framing Connection Experiments

Appendix A presents the force-displacement diagrams obtained from the monotonic STF connection experiments conducted on several material combinations. In general, slightly higher peak forces are observed for specimens loaded parallel to the grain. Exceptions occur in the datasets presented in Figure A1, where both loading directions exhibit nearly identical capacities, and in Figure A5, where the specimen loaded perpendicular to the grain shows a higher resistance. Overall, the observed behaviour of the tested configurations corresponds well with findings reported in the literature. For example, Vessby et al. [10] also reported similar responses, with peak capacities for both loading directions being relatively close to one another.

Appendix A.1. Partially Anchored Wall Diaphragms

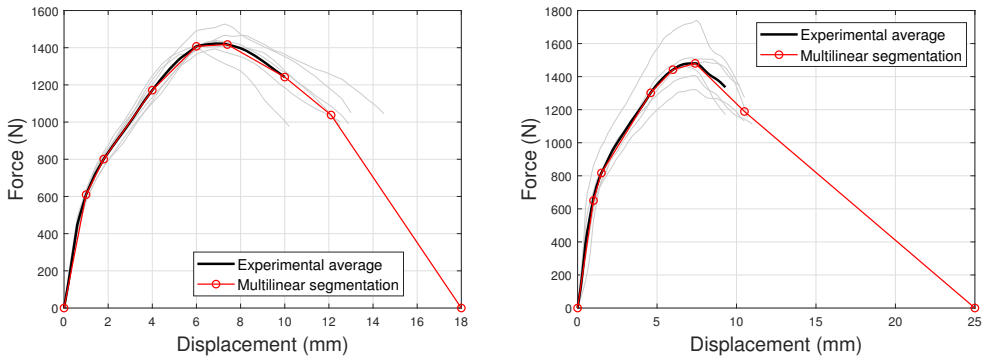

Figure A1. Multilinear segmentation of the experimental average, (**left**) parallel to the grain, and (**right**) perpendicular to the grain.

Appendix A.2. Fully Anchored Wall Diaphragms

Appendix A.2.1. Gypsum Plasterboard A and Staple Type a

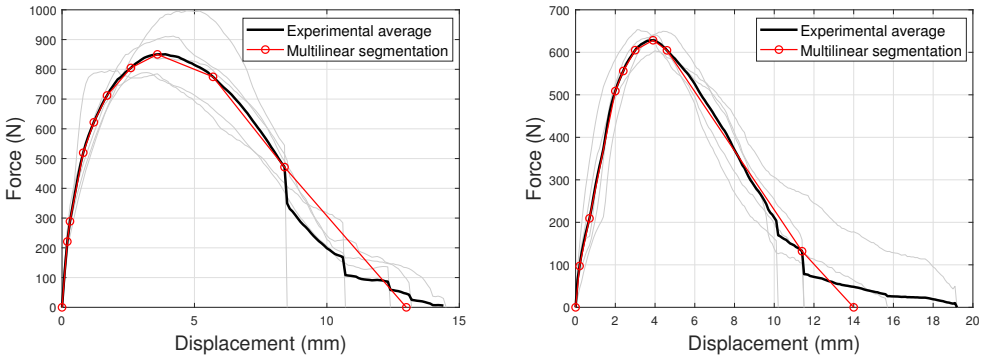

Figure A2. Multilinear segmentation of the experimental average, (**left**) parallel to the grain, and (**right**) perpendicular to the grain.

Appendix A.2.2. Gypsum Plasterboard B and Staple Type b

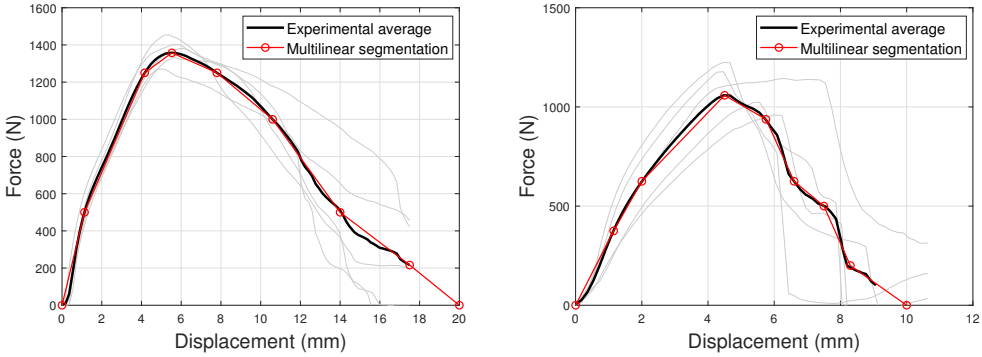

Figure A3. Multilinear segmentation of the experimental average, (**left**) parallel to the grain, and (**right**) perpendicular to the grain.

Appendix A.3. In-Plane Bending Resistance of Scaled Wall Diaphragms

Appendix A.3.1. Screwed Connections

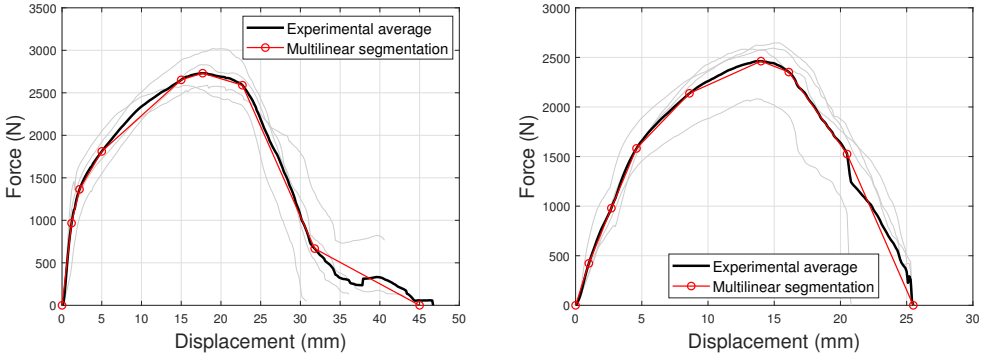

Figure A4. Multilinear segmentation of the experimental average, (**left**) parallel to the grain, and (**right**) perpendicular to the grain.

Appendix A.3.2. Stapled Connections

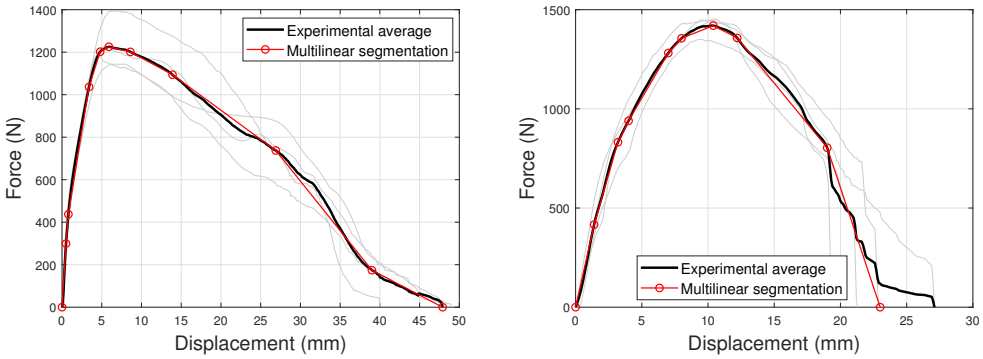

Figure A5. Multilinear segmentation of the experimental average, (**left**) parallel to the grain, and (**right**) perpendicular to the grain.

Appendix B. Stud-to-Rail (Withdrawal) Connection Experiments

The results, as shown in Figure A6, indicated that a single stud-to-rail connector exhibits high initial stiffness up to a displacement of approximately 0.2 mm. Beyond this point, the stiffness decreases steadily, allowing for greater displacement as softening behaviour becomes more prominent. Beyond a displacement of 0.2 mm, a slip is observed in the test data, which is likely attributable either to a malfunction of the testing machine or to inadequate clamping of the staple.

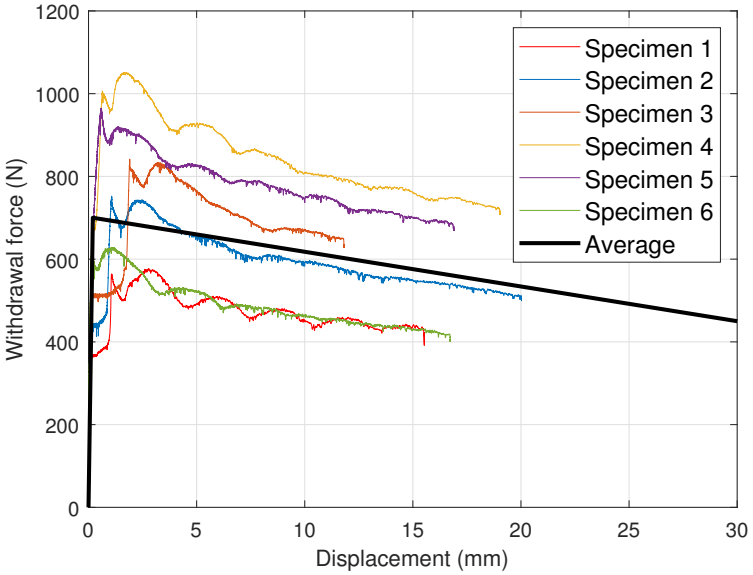

Figure A6. Force-displacement diagrams of the withdrawal experiments on a single connection as described in Section 3.

Appendix C. Visualisation of the Different Modelling Strategies

The figures below show the visualised responses of both FEM1 and FEM2. For FEM1 responses, a red circle (dot) indicates that the connection at that location has failed. For example, in Figure A7, in the bottom-left corner, failure is observed due to overloading of the staples at this location. Since FEM2 does not indicate failure, the occurring horizontal displacement of each connector is visualised. The sheathing panels in FEM2 appear to be modelled in a staggered pattern; however, this is to avoid overlap of semi-rigid links or of neighbouring panels.

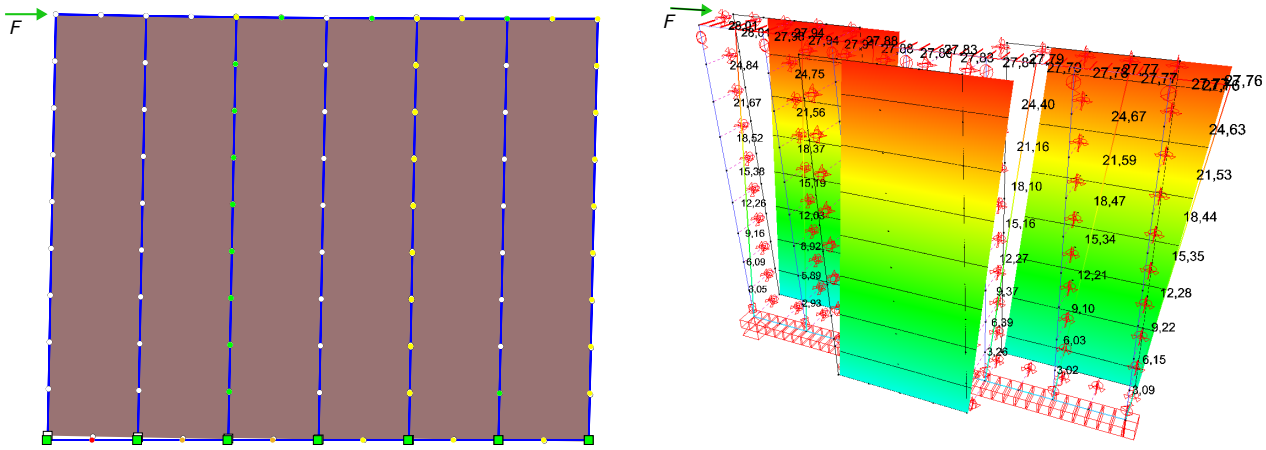

Figure A7. Visualisation of the FE response of the racking resistance test of partially anchored wall diaphragms. (**left**) FEM1, and (**right**) FEM2.

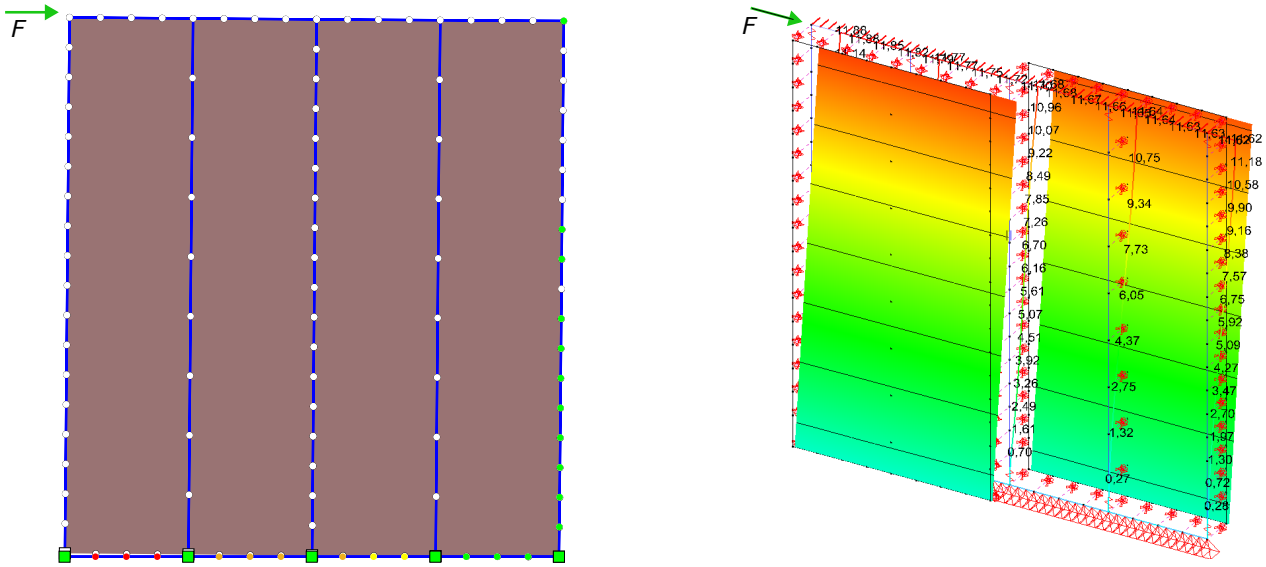

Figure A8. Visualisation of the FE response of the racking resistance test of fully anchored wall diaphragms. (**left**) FEM1, and (**right**) FEM2.

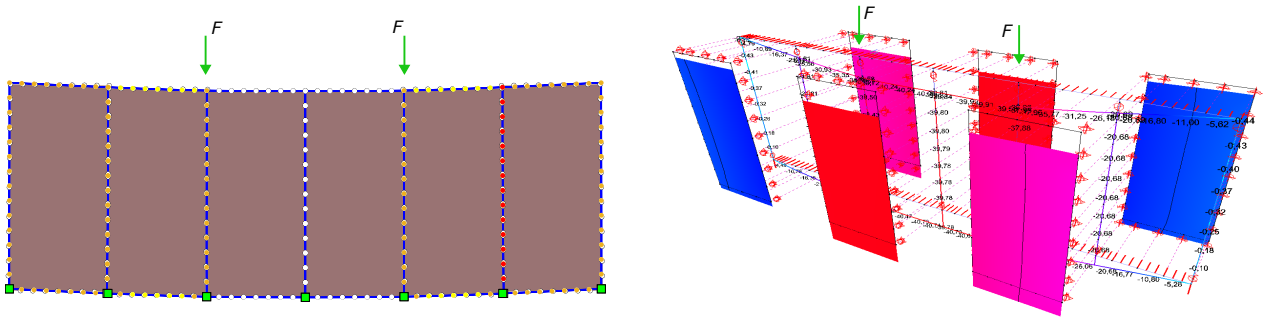

Figure A9. Visualisation of the FE response of the bending tests of the wall diaphragms. (**left**) FEM1, and (**right**) FEM2.

The visualised meshes are presented in Figures A10–A12. For FEM1, the mesh is generated automatically and is strongly governed by the distribution of the sheathing-to-framing (STF) connectors along the framing members. Each connector (spring element) defines a node with two translational degrees of freedom in both connected components. Between these connector nodes, the framing members are discretised using beam elements. The sheathing panels, modelled as plane-stress continuum elements, are meshed

in a rectangular pattern. The mesh geometry and boundary discretisation are therefore directly controlled by the connector locations, ensuring compatibility between the framing, connectors, and panel elements.

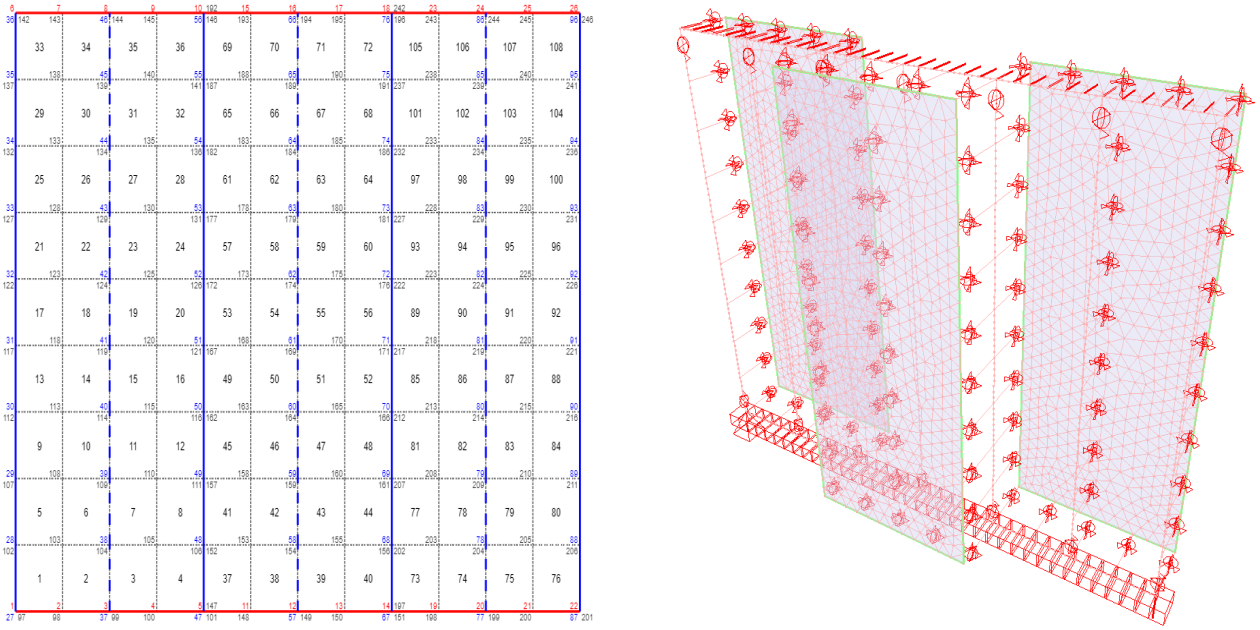

Figure A10. Visualisation of the FE mesh of the racking resistance test of partially anchored wall diaphragms. (**left**) FEM1, and (**right**) FEM2.

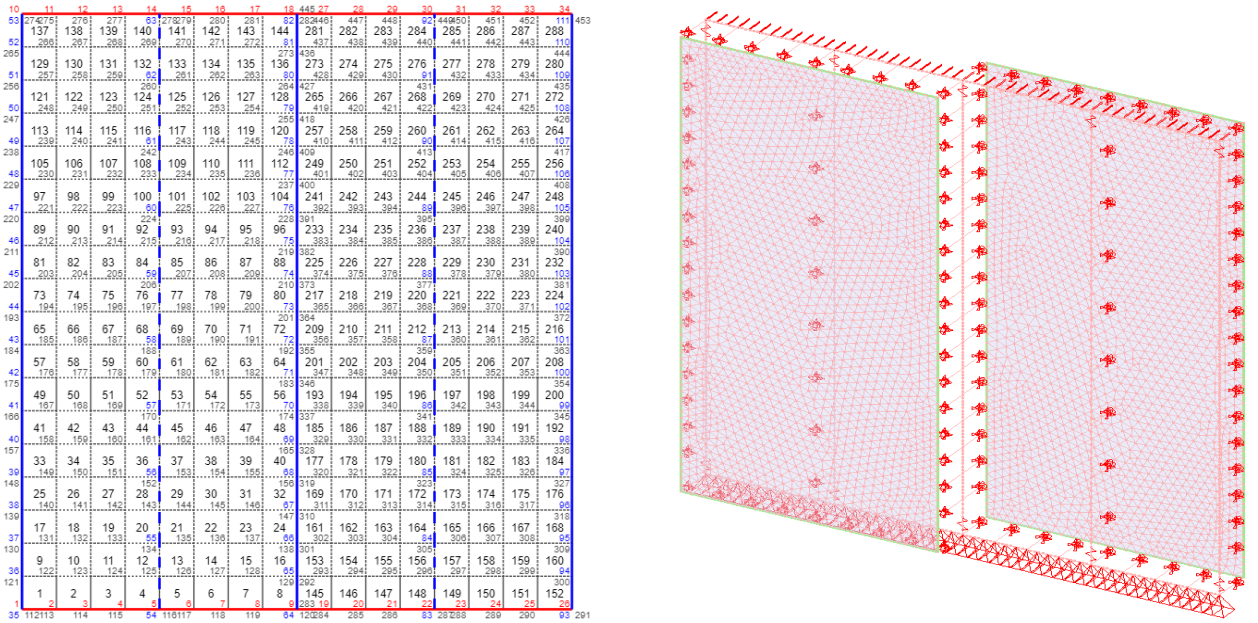

Figure A11. Visualisation of the FE mesh of the racking resistance test of fully anchored wall diaphragms. (**left**) FEM1, and (**right**) FEM2.

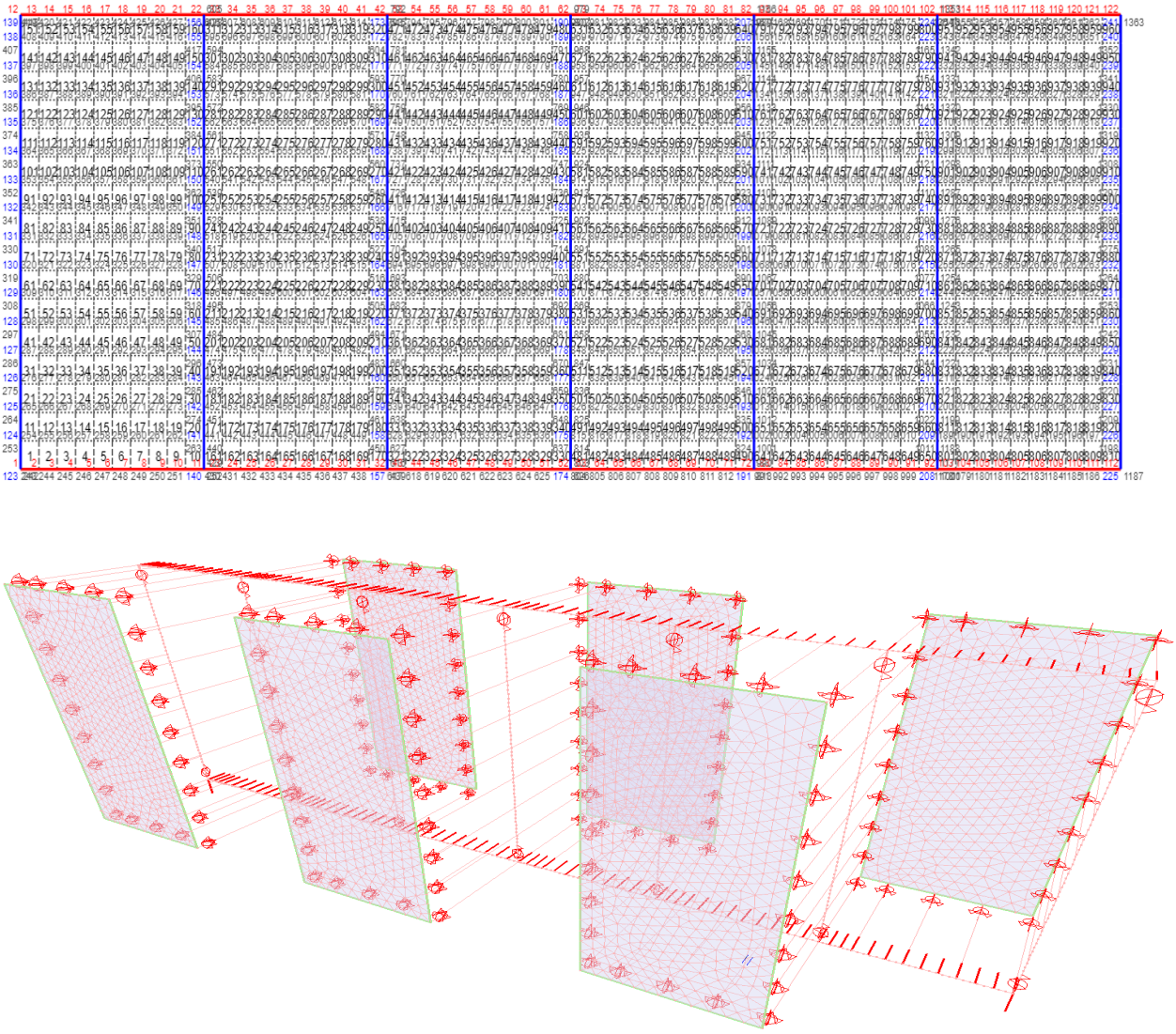

Figure A12. Visualisation of the FE mesh of the bending tests of the wall diaphragms. (**upper**) FEM1, and (**lower**) FEM2.

For FEM2, greater control over mesh adaptation is available. The software (Buildsoft Diamonds [35]) automatically subdivides each framing member into multiple rod elements, with element lengths depending on the connector spacing. Each connector is modelled as a semi-rigid link element. The sheathing panels, represented by shell elements, are discretised using a triangular mesh with a maximum element size of 0.05 m. This maximum element size was kept constant across all analyses and was selected based on mesh sensitivity studies, where it provided the most accurate and stable results.

References

1. Follesa, M.; Fragiacomo, M.; Casagrande, D.; Tomasi, R.; Piazza, M.; Vassallo, D.; Canetti, D.; Rossi, S. The new provisions for the seismic design of timber buildings in Europe. *Eng. Struct.* **2018**, *168*, 736–747. https://doi.org/10.1016/j.engstruct.2018.04.090.
2. Tupenaite, L.; Kanapeckiene, L.; Naimaviciene, J.; Kaklauskas, A.; Gecys, T. Timber Construction as a Solution to Climate Change: A Systematic Literature Review. *Buildings* **2023**, *13*, 976 https://doi.org/10.3390/buildings13040976.
3. Heräjärvi, H. Wooden buildings as carbon storages—Mitigation or oration? *Wood Mater. Sci. Eng.* **2019**, *14*, 291–297. https://doi.org/10.1080/17480272.2019.1635205.
4. Teischinger, A. Opportunities and limits of timber in construction. In Proceedings of the World Conference on Timber Engineering (WCTE 2016), Vienna, Austria, 22–25 August 2016.

5. Huber, J.A.; Ekevad, M.; Girhammar, U.A.; Berg, S. Structural robustness and timber buildings–a review. *Wood Mater. Sci. Eng.* **2019**, *14*, 107–128.
6. *EN-1995-1-1*: Eurocode 5: Design of Timber Structures—Part 1-1: General—Common Rules and Rules for Buildings. European Committee for Standardization: Brussels, Belgium, 2005.
7. *FprEN 1995-1-1:2025*; Eurocode 5—Design of Timber Structures—Part 1-1: General Rules and Rules for Buildings. European Committee for Standardization: Brussels, Belgium, 2025.
8. Vessby, J.; Källsner, B.; Olsson, A.; Girhammar, U.A. Evaluation of softening behaviour of timber light-frame walls subjected to in-plane forces using simple FE models. *Eng. Struct.* **2014**, *81*, 464–479. https://doi.org/10.1016/j.engstruct.2014.09.032.
9. Judd, J.P.; Fonseca, F.S. Analytical Model for Sheathing-to-Framing Connections in Wood Shear Walls and Diaphragms. *J. Struct. Eng.* **2005**, *131*, 345–352. https://doi.org/10.1061/(asce)0733-9445(2005)131:2(345).
10. Vessby, J.; Serrano, E.; Olsson, A. Coupled and uncoupled nonlinear elastic finite element models for monotonically loaded sheathing-to-framing joints in timber based shear walls. *Eng. Struct.* **2010**, *32*, 3433–3442. https://doi.org/10.1016/j.engstruct.2010.05.018.
11. Humbert, J.; Boudaud, C.; Baroth, J.; Hameury, S.; Daudeville, L. Joints and wood shear walls modelling I: Constitutive law, experimental tests and FE model under quasi-static loading. *Eng. Struct.* **2014**, *65*, 52–61. https://doi.org/10.1016/j.engstruct.2014.01.047.
12. Schweigler, M.; Bader, T.K.; Hochreiner, G. Engineering modeling of semi-rigid joints with dowel-type fasteners for nonlinear analysis of timber structures. *Eng. Struct.* **2018**, *171*, 123–139. https://doi.org/10.1016/j.engstruct.2018.05.063.
13. Kuai, L.; Ormarsson, S.; Vessby, J.; Maharjan, R. A numerical and experimental investigation of non-linear deformation behaviours in light-frame timber walls. *Eng. Struct.* **2022**, *252*, 113599. https://doi.org/10.1016/j.engstruct.2021.113599.
14. Kuai, L.; Ormarsson, S.; Vessby, J. Nonlinear FE-analysis and testing of light-frame timber shear walls subjected to cyclic loading. *Constr. Build. Mater.* **2023**, *362*, 129646. https://doi.org/10.1016/j.conbuildmat.2022.129646.
15. Loo, W.Y.; Quenneville, P.; Chouw, N. A numerical approach for simulating the behaviour of timber shear walls. *Struct. Eng. Mech.* **2012**, *42*, 383–407. https://doi.org/10.12989/sem.2012.42.3.383.
16. Véliz, F.; Chacón, M.F.; Lagos, J.; Berwart, S.; López, N.; Guindos, P. Structural performance of strong timber diaphragms: High-capacity light-timber frames and cross-laminated timber. *Structures* **2024**, *63*, 106335. https://doi.org/10.1016/j.istruc.2024.106335.
17. Gattesco, N.; Boem, I. Stress distribution among sheathing-to-frame nails of timber shear walls related to different base connections: Experimental tests and numerical modelling. *Constr. Build. Mater.* **2016**, *122*, 149–162. https://doi.org/10.1016/j.conbuildmat.2016.06.079.
18. Hassanieh, A.; Valipour, H. Experimental and numerical study of OSB sheathed-LVL stud wall with stapled connections. *Constr. Build. Mater.* **2020**, *233*, 117373. https://doi.org/10.1016/j.conbuildmat.2019.117373.
19. Wang, S.; Lin, J.; Dong, S.; Chen, Z.; Kong, F.; Ma, P.; Wang, F.; Que, Z. Lateral resistance performance of wood-frame shear walls with wooden nail connections: Experimental and finite element analysis. *J. Bioresour. Bioprod.* **2025**, *10*, 410–424. https://doi.org/10.1016/j.jobab.2025.04.002.
20. Kuai, L.; Ormarsson, S.; Vessby, J. Numerical and experimental investigations of prefabricated light-frame timber modules. *Eng. Struct.* **2024**, *303*, 117528. https://doi.org/10.1016/j.engstruct.2024.117528.
21. Estrella, X.; Guindos, P.; Almazán, J.L.; Malek, S. Efficient nonlinear modeling of strong wood frame shear walls for mid-rise buildings. *Eng. Struct.* **2020**, *215*, 110670. https://doi.org/10.1016/j.engstruct.2020.110670.
22. Pintarič, K.; Premrov, M. Mathematical modelling of timber-framed walls using fictive diagonal elements. *Appl. Math. Model.* **2013**, *37*, 8051–8059. https://doi.org/10.1016/j.apm.2013.02.050.
23. Moroder, D. Floor Diaphragms in Multi-Storey Timber Buildings. Ph.D. Thesis, University of Canterbury, Christchurch, New Zealand, 2016.
24. Vogrinec, K.; Premrov, M.; Šilih, E.K. Simplified modelling of timber-framed walls under lateral loads. *Eng. Struct.* **2016**, *111*, 275–284. https://doi.org/10.1016/j.engstruct.2015.12.029.
25. Vogrinec, K.; Premrov, M. Influence of the design approach on the behaviour of timber-frame panel buildings under horizontal forces. *Eng. Struct.* **2018**, *175*, 1–12. https://doi.org/10.1016/j.engstruct.2018.08.014.
26. Premrov, M.; Ber, B.; Šilih, E.K. Study of load-bearing timber-wall elements using experimental testing and mathematical modelling. *Adv. Prod. Eng. Manag.* **2021**, *16*, 67–81. https://doi.org/10.14743/apem2021.1.385.
27. Premrov, M.; Šilih, E.K. Numerical Analysis of the Racking Behaviour of Multi-Storey Timber-Framed Buildings Considering Load-Bearing Function of Double-Skin Façade Elements. *Sustainability* **2023**, *15*, 6379. https://doi.org/10.3390/su15086379.
28. Premrov, M.; Šilih, E.K. Numerical Study on In-Plane Behaviour of Light Timber-Framed Wall Elements Under a Horizontal Load Impact. *Buildings* **2025**, *15*, 778. https://doi.org/10.3390/buildings15050778.
29. Steensels, R.; De Proft, K.; Vandoren, B. Experimental and analytical assessment of racking resistance of partially anchored timber frame walls. *Int. J. Comput. Methods Exp. Meas.* **2017**, *5*, 847–857. https://doi.org/10.2495/CMEM-V5-N6-847-857.

30. Byloos, D.; Vandoren, B. Experimental and analytical assessment of the racking behavior of timber frame walls with single-sided double-layered sheathing panels. *Eng. Struct.* **2024**, *316*, 118592. https://doi.org/10.1016/j.engstruct.2024.118592.
31. Byloos, D.; Engelen, T.; Vandoren, B. Experimental and analytical assessment of the combined in-plane bending-shear behavior of timber frame walls. *Eng. Struct.* **2025**, *343*, 121068. https://doi.org/10.1016/j.engstruct.2025.121068.
32. Yunhua, L.; Eriksson, A. Extension of field consistence approach into developing plane stress elements. *Comput. Methods Appl. Mech. Eng.* **1999**, *173*, 111–134.
33. *NBN-EN-1381*; Tests Methods Load Bearing Stapled Joints. European Committee for Standardization: Brussels, Belgium, 2016.
34. Borst, R.D.; Crisfield, M.A.; J.C.Remmers, J.; V.Verhoorsel, C. *Non-Linear Finite Element Analysis of Solids and Structures*; Wiley: Hoboken, NJ, USA, 2012; Chapter 6: Damage Mechanics.
35. *Buildsoft Diamonds 2026*; Buildsoft: Merelbeke-Melle, Belgium, 2026.
36. *EN-312*; Particleboards—Specifications. European Committee for Standardization: Brussels, Belgium, 2010.
37. *EN-594*; Timber Structures, Test Methods—Racking Strength and Stiffness of Timber Frame Wall Panels. European Committee for Standardization: Brussels, Belgium, 2011.
38. *EN-520+A1*; Gypsum Plasterboards-Definitions, Requirements and Test Methods. European Committee for Standardization: Brussels, Belgium, 2009.